Research Article | Vol. 34, No. 5 / 9 Mar 2026 / Optics Express 9207

Optics EXPRESS

Physics-informed finite element multi-scale modeling of light propagation using numerical approximation of slowly varying envelope

JINGWEI WANG,[1,2,†] FAN XIAO,[1,†] ZHANGWEI YU,[1,3,5] KUN LIANG,[2] AND YUNTIAN CHEN[1,2,4,6]

[1] *School of Optical and Electronic Information, Huazhong University of Science and Technology, Wuhan 430074, China*
[2] *School of Electronic Information and Communications, Huazhong University of Science and Technology, Wuhan 430074, China*
[3] *Hangzhou Institute of Advanced Studies, Zhejiang Normal University, 1108 Geng Wen Road, Hangzhou 311231, China*
[4] *Wuhan National Laboratory of Optoelectronics, Huazhong University of Science and Technology, Wuhan 430074, China*
[5] *yuzhangwei@zjnu.cn*
[6] *yuntian@hust.edu.cn*
[†] The authors contributed equally to this work.

Abstract: In this paper, we extend the numerical techniques based on the slow envelope approximation in the finite element method by introducing physical information into the construction of multi-scale basis functions for scenarios where the wave effects matter. Thereby, the proposed method here enables the modeling and simulation of multi-scale optical devices and systems, especially those that involve strong wave effects. Various multi-scale basis function construction techniques have been developed, tailored to different physical scenarios of strong wave effects, to achieve precise and efficient computation. Without loss of generality, the accuracy and efficiency of the method are verified by computing double-slit interference, off-axis reflective systems, and refractive-diffractive hybrid optical systems. These results show that this method can be applied to various scenarios, such as refraction, multiple reflection, and multi-beam diffraction, while it can achieve an order of magnitude improvement in calculation speed compared with the standard finite element method.

© 2026 Optica Publishing Group under the terms of the Optica Open Access Publishing Agreement

1. Introduction

Multi-scale modeling of light propagation, which provides valuable insights into light scattering phenomena in complex structures and simultaneously drives advancements in cutting-edge technologies such as augmented/virtual reality (AR/VR) systems [1–4], light detection and ranging (LiDAR) devices [5,6], and various metamaterial-based optical components, has received considerable attention recently. This is due to the fact that state-of-the-art photonic devices/systems usually operate across wavelength scale to geometric-optics length scale, which cannot be modeled solely by either full-wave modeling methods, i.e., Finite Difference Time Domain (FDTD) [7] and Finite Element Method (FEM) [8,9], or geometric optics modeling like Ray-Tracing (RT) technique [10]. To address this problem, the current mainstream solution involves hybrid methods [11–15], which segment the optical system into sub-regions according to feature size and apply different numerical algorithms to each sub-region, with data exchanged using predefined files. For example, Leiner et al. combined RT with FDTD [11,16–18]. Ziga Lokar et al. combined Rigorous Coupled Wave Analysis (RCWA), RT and transfer matrix method to simulate solar cells [12,19]. Wyrowski et al. integrated the Fourier transform with RT to solve the electric field of micro-nano structures [13–15,20,21].

#579547 https://doi.org/10.1364/OE.579547
Journal © 2026 Received 18 Sep 2025; revised 25 Jan 2026; accepted 6 Feb 2026; published 6 Mar 2026

The rigorous hybrid method needs to construct a precise mapping, which is overlooked in the aforementioned literature [11,12,16–21], between the optical fields calculated from full-wave modeling and the ray bundles obtained from geometric optics modeling. To bypass such precise ray-wave mapping, we have proposed a unified Ray-Wave Method (RWM) [22], in which the wavefront information calculated from geometric optics modeling is embedded into the full-wave FEM modeling via multi-scale basis functions, as demonstrated in Fig. 1(a). Our preliminary work, see details in the paper [22], has validated its effectiveness and efficiency. However, the current RWM only uses a single type of multi-scale basis function to discretize the electric field. This method fails in situations with strong wave effects, i.e., interference or the co-existence of multiple beams/reflections. In contrast to refraction and self-focusing considered in previous work [22], strong wave effects cause light waves to propagate in multiple directions, leading to significant field variation in local regions. In those regions, the geometric optics method under single wavefront approximation cannot accurately account for the phase gradient of the superposition of light waves, and thus is inadequate to construct multi-scale basis functions. To overcome this issue, it is essential to integrate the physical information of strong wave effects into the multi-scale basis functions, which are tailored to specific physical scenarios. The challenge

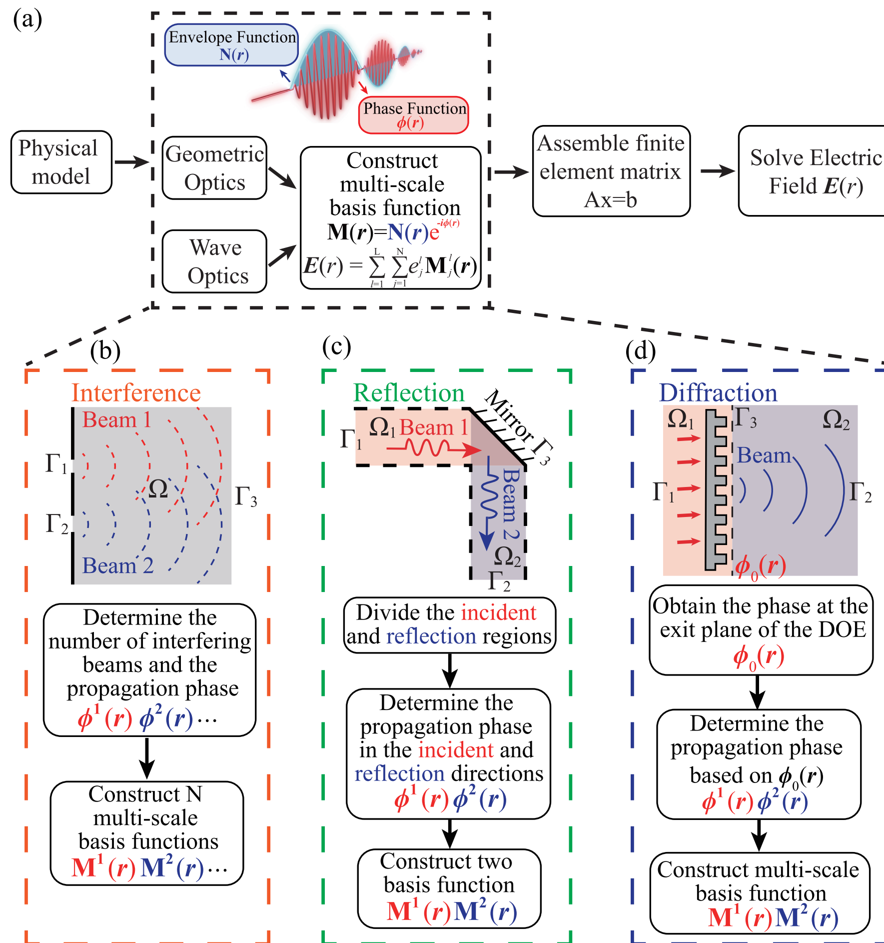

Fig. 1. (a) Schematic diagram of RWM principle and workflow. (b)-(d) Handling and construction of multi-scale basis functions in interference/reflection/diffraction problems.

Optics EXPRESS

lies in constructing appropriate multi-scale basis functions and unifying the treatment of various optical phenomena under RWM.

This work introduces a physics-informed concept [23–27] to construct multi-scale basis functions for different scenarios, especially for those with strong wave effects. In fact, the slowly varying envelope approximation (SVEA) in FEM inherently constitutes a physics-informed numerical scheme, relying on predefined knowledge of wave propagation directions, and RWM extends this concept into a generalized framework. Here, we move one step further to account for the strong wave effects under RWM by carefully analyzing the physical phenomena of strong wave effects, such as interference, reflection, and diffraction. Specifically, we construct multi-scale basis functions that incorporate the corresponding physical information. As for interference scenario with multiple incident waves, the multi-scale basis functions are expanded and set to establish one-to-one correspondence with each incident wave. As for reflection scenario, the whole computation is decomposed according to the reflected beams, wherein each subdomain contains only unidirectional propagating beam coupling at reflective interfaces. Regarding diffraction induced by diffractive optical elements (DOEs), where beam separation proves challenging due to the coexistence of multiple diffraction orders, our approach involves phase profile computation at the exit plane of the DOEs followed by construction of corresponding multi-scale basis function for subsequent simulation. These schemes enhance the applicability of RWM, achieving high numerical accuracy comparable to full-wave modeling in a variety of complex scenarios while significantly improving computational speed by an order of magnitude and reducing memory usage.

This paper has a total of four sections. Section 2 introduces RWM for addressing strong wave effects and the construction of multi-scale basis functions based on physical information for different problems in detail. In Section 3, we apply RWM to simulate several examples and compare the results with the standard FEM. Finally, the conclusion is reached in Section 4.

2. Theory and methods

In the presence of strong wave effect, the electric field continues to satisfy the vector wave equation

$$\nabla \times \boldsymbol{\mu}_r^{-1}(\boldsymbol{r})\nabla \times \boldsymbol{E}(\boldsymbol{r}) - k_0^2 \boldsymbol{\epsilon}_r(\boldsymbol{r})\boldsymbol{E}(\boldsymbol{r}) = 0, \tag{1}$$

where $\boldsymbol{E}(\boldsymbol{r})$ is the electric field, $\boldsymbol{\epsilon}_r(\boldsymbol{r})/\boldsymbol{\mu}_r(\boldsymbol{r})$ represents the relative permittivity/permeability of the medium, $k_0 = 2\pi/\lambda_0$, where k_0 and λ_0 represent the wave number and wavelength in free space, respectively. When a single beam experiences refraction or self-focusing, it continues to propagate in a specific direction. The propagation phase $\phi(\boldsymbol{r})$ of the electric field $\boldsymbol{E}(\boldsymbol{r})$ can be accurately computed using the Fast Iterative Method (FIM) [28–30]. In this case, $\boldsymbol{E}(\boldsymbol{r})$ can be discretized precisely using one type of multi-scale basis function, expressed as $\boldsymbol{E}(\boldsymbol{r}) = \sum_{j=1}^{N} e_j \boldsymbol{M}_j(\boldsymbol{r})$. Subsequently, the standard FEM procedure is implemented to assemble the matrix, facilitating the computation of the electric field $\boldsymbol{E}(\boldsymbol{r})$. For more information about the multi-scale basis function, please refer to References [9,22]. However, when strong wave effects, such as diffraction, are involved, the behavior of the beam becomes more complex. To accurately discretize the electric field using multi-scale basis functions, appropriate processing methods are necessary.

The application of RWM in analyzing optical phenomena relies fundamentally on the development of multi-scale basis functions that comply with physical principles. These functions are essential for accurately discretizing the electric field and for reducing the degrees of freedom (DOFs) in the solution process. Unlike refraction and self-focusing, which utilize only one type of multi-scale basis function, interference and reflection require two or more types, while multi-beam diffraction involves more complex beam evolution and propagation phases. In this work, we extend the discretized form of the electric field to a form that includes multiple types of

basis functions,

$$\boldsymbol{E}(\boldsymbol{r}) = \sum_{l=1}^{L} \sum_{j=1}^{N_l} e_j^l \boldsymbol{M}_j^l(\boldsymbol{r}), \tag{2}$$

where the superscript l denotes the type of multi-scale basis function, L represents the total number of types of multi-scale basis functions, the subscript j indicates the index within a given type l of multi-scale basis function, and N_l signifies the number of basis functions in type l. Due to the inherent limitations of the eikonal equation, the propagation phases and multi-scale basis functions for these more complex situations cannot be directly calculated through the FIM and require additional processing. Essentially, the physical information of the multi-scale light propagation is encoded in how the different types of multi-scale basis function are determined, which will be elaborated shortly. The practical implementation of RWM for handling interference, reflection, and diffraction can be summarized in the following 5 steps,

1. Physical model is developed to integrate geometry, material properties, and boundary conditions.
2. Identify the type of optical wave behavior, as interference, reflection, and diffraction each require distinct approaches.
3. Construct multi-scale basis functions specifically tailored to the optical phenomenon, and use these functions to discretize the electric field.
4. Assemble the finite element matrix based on basis functions and specific boundary conditions.
5. Solve the finite element matrix to obtain the electric field of the physical model.

In the following subsections, RWM for interference, reflection, and diffraction will be introduced in sequence, with a focus on constructing multi-scale basis functions and matrix assembly.

2.1. Interference

Interference involves a superposition of two or more coherent light beams in space based on their phase relationships. It is fundamentally the linear superposition of the electric fields in the complex domain, without generating new beams. As illustrated in Fig. 1(b), the construction of multi-scale basis functions for the interference of two beams consists of two steps. First, one determines the number of coherent light beams and uses the FIM to calculate the propagation phases $\phi^1(\boldsymbol{r})$ and $\phi^2(\boldsymbol{r})$ of these beams. Second, one constructs the multi-scale basis functions $\boldsymbol{M}_j^1(\boldsymbol{r}) = \boldsymbol{N}_j^1(\boldsymbol{r})e^{-i\phi^1(\boldsymbol{r})}$ and $\boldsymbol{M}_j^2(\boldsymbol{r}) = \boldsymbol{N}_j^2(\boldsymbol{r})e^{-i\phi^2(\boldsymbol{r})}$ to represent the discretize coherent beams $\boldsymbol{E}^1(\boldsymbol{r}) = \sum_{j=1}^{N} e_j^1 \boldsymbol{M}_j^1(\boldsymbol{r})$ and $\boldsymbol{E}^2(\boldsymbol{r}) = \sum_{j=1}^{N} e_j^2 \boldsymbol{M}_j^2(\boldsymbol{r})$, respectively. The superscript $(1, 2)$ indicates different beams, while the subscript N represents the number of basis functions used for discretization. The total electric field is then given by $\boldsymbol{E}(\boldsymbol{r}) = \boldsymbol{E}^1(\boldsymbol{r}) + \boldsymbol{E}^2(\boldsymbol{r})$.

The assembly matrix is derived using examples of scattering boundary conditions (SBC) and the plane wave incident excitation. As shown in Fig. 1(b), Ω is the computational domain, and the boundary Γ consists of Γ_1, Γ_2, and Γ_3. Here, Γ_1 and Γ_2 correspond to the incidences of light beam 1 and light beam 2, respectively, satisfying

$$\boldsymbol{n} \times \nabla \times \boldsymbol{E}^1(\boldsymbol{r}) = ik_0\boldsymbol{n} \times \boldsymbol{E}^1(\boldsymbol{r}) \times \boldsymbol{n} - \boldsymbol{n} \times [\boldsymbol{E}^{1,inc}(\boldsymbol{r}) \times ik(\boldsymbol{n} - \boldsymbol{k}^{1,inc})]e^{-ik\boldsymbol{k}^{1,inc}\cdot\boldsymbol{r}} \quad on\Gamma_1, \tag{3a}$$

$$\boldsymbol{n} \times \nabla \times \boldsymbol{E}^2(\boldsymbol{r}) = ik_0\boldsymbol{n} \times \boldsymbol{E}^2(\boldsymbol{r}) \times \boldsymbol{n} - \boldsymbol{n} \times [\boldsymbol{E}^{2,inc}(\boldsymbol{r}) \times ik(\boldsymbol{n} - \boldsymbol{k}^{2,inc})]e^{-ik\boldsymbol{k}^{2,inc}\cdot\boldsymbol{r}} \quad on\Gamma_2, \tag{3b}$$

where $\boldsymbol{n}$ represents the outward unit normal vector of the boundary, k is the wave number, $\boldsymbol{E}^{(1,2),inc}(\boldsymbol{r})$ represents the electric field intensity of the incident beam $(1, 2)$, and $\boldsymbol{k}^{(1,2),inc}$ represents

the incident direction of the incident beam (1, 2). The boundary Γ_3 represents the scattering boundary condition, which satisfies

$$\boldsymbol{n} \times \nabla \times (\boldsymbol{E}^1(\boldsymbol{r}) + \boldsymbol{E}^2(\boldsymbol{r})) - ik_0\boldsymbol{n} \times [\boldsymbol{E}^1(\boldsymbol{r}) + \boldsymbol{E}^2(\boldsymbol{r})] \times \boldsymbol{n} = 0 \quad on\Gamma_3. \tag{4}$$

By substituting the discrete form of the electric field into Eqs. (1,3a,3b,4) adhering to standard finite element procedures, we can derive the following matrix form,

$$\begin{bmatrix} A^1 + K^1 & T^1 \\ T^2 & A^2 + K^2 \end{bmatrix} \begin{bmatrix} x^1 \\ x^2 \end{bmatrix} = \begin{bmatrix} b^1 \\ b^2 \end{bmatrix}, \tag{5}$$

where A^1, A^2, K^1, K^2, T^1 and T^2 are $N \times N$ matrices, with matrix elements represented as

$$\begin{cases} A^1_{ij} = \int_\Omega [\nabla \times (\boldsymbol{M}^1_i)^* \cdot \nabla \times \boldsymbol{M}^1_j - k_0^2\epsilon_r(\boldsymbol{M}^1_i)^* \cdot \boldsymbol{M}^1_j]dV, \\ A^2_{ij} = \int_\Omega [\nabla \times (\boldsymbol{M}^2_i)^* \cdot \nabla \times \boldsymbol{M}^2_j - k_0^2\epsilon_r(\boldsymbol{M}^2_i)^* \cdot \boldsymbol{M}^2_j]dV, \\ K^1_{ij} = \int_{\Gamma_1+\Gamma_2+\Gamma_3} [ik_0(\boldsymbol{M}^1_i)^* \cdot \boldsymbol{M}^1_j]dS, \\ K^2_{ij} = \int_{\Gamma_1+\Gamma_2+\Gamma_3} [ik_0(\boldsymbol{M}^2_i)^* \cdot \boldsymbol{M}^2_j]dS, \\ T^1_{ij} = \int_{\Gamma_1+\Gamma_2+\Gamma_3} [ik_0(\boldsymbol{M}^1_i)^* \cdot \boldsymbol{M}^2_j - (\boldsymbol{M}^1_i)^* \cdot \boldsymbol{n} \times \nabla \times \boldsymbol{M}^2_j]dS, \\ T^2_{ij} = \int_{\Gamma_1+\Gamma_2+\Gamma_3} [ik_0(\boldsymbol{M}^2_i)^* \cdot \boldsymbol{M}^1_j - (\boldsymbol{M}^2_i)^* \cdot \boldsymbol{n} \times \nabla \times \boldsymbol{M}^1_j]dS. \end{cases}$$

b^1 and b^2 are $N \times 1$ vectors, with vector elements represented as

$$\begin{cases} b^1_i = \int_{\Gamma_1} (\boldsymbol{M}^1_i)^* \cdot \boldsymbol{n} \times [\boldsymbol{E}^{1,inc}(\boldsymbol{r}) \times ik(\boldsymbol{n} - \boldsymbol{k}^{1,inc})]e^{-ik\boldsymbol{k}^{1,inc}\cdot\boldsymbol{r}}dS \\ \quad + \int_{\Gamma_2} (\boldsymbol{M}^1_i)^* \cdot \boldsymbol{n} \times [\boldsymbol{E}^{2,inc}(\boldsymbol{r}) \times ik(\boldsymbol{n} - \boldsymbol{k}^{2,inc})]e^{-ik\boldsymbol{k}^{2,inc}\cdot\boldsymbol{r}}dS, \\ b^2_i = \int_{\Gamma_2} (\boldsymbol{M}^2_i)^* \cdot \boldsymbol{n} \times [\boldsymbol{E}^{2,inc}(\boldsymbol{r}) \times ik(\boldsymbol{n} - \boldsymbol{k}^{2,inc})]e^{-ik\boldsymbol{k}^{2,inc}\cdot\boldsymbol{r}}dS \\ \quad + \int_{\Gamma_1} (\boldsymbol{M}^2_i)^* \cdot \boldsymbol{n} \times [\boldsymbol{E}^{1,inc}(\boldsymbol{r}) \times ik(\boldsymbol{n} - \boldsymbol{k}^{1,inc})]e^{-ik\boldsymbol{k}^{1,inc}\cdot\boldsymbol{r}}dS. \end{cases}$$

$x^1 = \{e^1_j\}$ and $x^2 = \{e^2_j\}$ is the coefficient column vector to be determined.

Solving the Eq. (5) can get the electric field of two light beams that lead to interference. Consistent with the refractive case [22], this work also assigns polynomial basis functions to be at least quadratic to effectively reduce dispersion errors. And the numerical integration accuracy is ensured by fourth-order Gaussian integration. The interference case incorporates at least two types of multi-scale basis functions, resulting in doubled DOFs in comparison with that of the refractive case, yet still significantly less than that in standard FEM.

2.2. Reflection

We take the reflection involving two beams as the second example, the incident beam $\boldsymbol{E}^1(\boldsymbol{r})$ and the reflected beam $\boldsymbol{E}^2(\boldsymbol{r})$ produced by the reflection of the incident beam $\boldsymbol{E}^1(\boldsymbol{r})$. These two beams are linearly superimposed near the reflective surface Γ_3, forming localized standing waves

without generating additional beams. Furthermore, the transmission directions and working domains of the two beams differ on either side of the reflective surface. As illustrated in Fig. 1(c), the construction of multi-scale basis functions for reflection involves the following three steps. First, one divides the computational domain into two subdomains, red(Ω_1) and blue(Ω_2), based on the working domains of the incident and reflected beams. These domains are delineated by the reflective surface and partially overlap. Second, one uses FIM to calculate the propagation phases $\phi^1(\boldsymbol{r})$ and $\phi^2(\boldsymbol{r})$ for the incident and reflected beams, respectively, based on the characteristics of the incident beams and the reflective surface. Third, one independently constructs the multi-scale basis functions $\boldsymbol{M}_j^1(\boldsymbol{r}) = \boldsymbol{N}_j^1(\boldsymbol{r})e^{-i\phi^1(\boldsymbol{r})}$ and $\boldsymbol{M}_j^2(\boldsymbol{r}) = \boldsymbol{N}_j^2(\boldsymbol{r})e^{-i\phi^2(\boldsymbol{r})}$ for discretizing the incident beam $\boldsymbol{E}^1(\boldsymbol{r}) = \sum_{j=1}^{N_1} e_j^1\boldsymbol{M}_j^1(\boldsymbol{r})$ and the reflected beam $\boldsymbol{E}^2(\boldsymbol{r}) = \sum_{j=1}^{N_2} e_j^2\boldsymbol{M}_j^2(\boldsymbol{r})$. The working domains of these basis functions correspond to the Ω_1 and Ω_2 defined in the first step.

Since the incident beam and the reflected beam are linearly superimposed, Eq. (1) can be rewritten in the following form

$$\nabla \times \boldsymbol{\mu}_r^{-1}(\boldsymbol{r})\nabla \times \boldsymbol{E}^1(\boldsymbol{r}) - k_0^2\boldsymbol{\epsilon}_r(\boldsymbol{r})\boldsymbol{E}^1(\boldsymbol{r}) = 0 \quad on \quad \Omega_1, \tag{6a}$$

$$\nabla \times \boldsymbol{\mu}_r^{-1}(\boldsymbol{r})\nabla \times \boldsymbol{E}^2(\boldsymbol{r}) - k_0^2\boldsymbol{\epsilon}_r(\boldsymbol{r})\boldsymbol{E}^2(\boldsymbol{r}) = 0 \quad on \quad \Omega_2, \tag{6b}$$

$$\boldsymbol{n} \times (\boldsymbol{E}^1(\boldsymbol{r}) + \boldsymbol{E}^2(\boldsymbol{r})) = 0 \quad on \quad \Gamma_3, \tag{6c}$$

where Γ_3 represents the boundary of the reflective surface. To simplify the processing, it is assumed that the reflection is ideal mirror reflection, employing the perfect electric conductor (PEC) boundary condition as described in Eq. (6c).

Both the incident and reflected beams adhere to the vector wave equation within their working domains and satisfy the reflection condition at Γ_3. The derivation of the assembly matrix also incorporates examples of SBC on Γ_2 and plane wave incident excitations on Γ_1. The application of the standard finite element procedure to Eqs. (6a) and (6b) results in

$$Ax = b, \tag{7}$$

where the stiffness matrix is expressed as $A = \begin{bmatrix} A^1 + K^1 & 0 \\ 0 & A^2 + K^2 \end{bmatrix}$, A^1 and K^1 are $N_1 \times N_1$ matrices, A^2 and K^2 are $N_2 \times N_2$ matrices, the matrix elements are represented as

$$\begin{cases} A_{ij}^1 = \int_{\Omega_1} [\nabla \times (\boldsymbol{M}_i^1)^* \cdot \nabla \times \boldsymbol{M}_j^1 - k_0^2\epsilon_r(\boldsymbol{M}_i^1)^* \cdot \boldsymbol{M}_j^1]dV, \\ K_{ij}^1 = \int_{\Gamma_1} [ik_0(\boldsymbol{M}_i^1)^* \cdot \boldsymbol{M}_j^1]dS, \\ A_{ij}^2 = \int_{\Omega_2} [\nabla \times (\boldsymbol{M}_i^2)^* \cdot \nabla \times \boldsymbol{M}_j^2 - k_0^2\epsilon_r(\boldsymbol{M}_i^2)^* \cdot \boldsymbol{M}_j^2]dV, \\ K_{ij}^2 = \int_{\Gamma_2} [ik_0(\boldsymbol{M}_i^2)^* \cdot \boldsymbol{M}_j^2]dS, \end{cases}$$

the load vector $b = \begin{bmatrix} b^1 & 0 \end{bmatrix}^T$, $b_i^1 = \int_{\Gamma_1} (\boldsymbol{M}_i^1)^* \cdot \boldsymbol{n} \times [\boldsymbol{E}^{inc}(\boldsymbol{r}) \times ik(\boldsymbol{n} - \boldsymbol{k}^{inc})]e^{-ik\boldsymbol{k}^{inc}\cdot\boldsymbol{r}}dS$, the coefficient $x = \begin{bmatrix} x^1 & x^2 \end{bmatrix}^T$, $x^1 = \begin{bmatrix} x^1_{\Omega_1-\Gamma_3} & x^1_{\Gamma_3} \end{bmatrix}^T$, and $x^2 = \begin{bmatrix} x^2_{\Omega_2-\Gamma_3} & x^2_{\Gamma_3} \end{bmatrix}^T$. The subscript $\Omega_1-\Gamma_3/\Omega_2-\Gamma_3/\Gamma_3$ represents the region where the coefficients to be determined are located. $\Omega_1 - \Gamma_3(\Omega_2 - \Gamma_3)$ denotes the domain $\Omega_1(\Omega_2)$ with the boundary Γ_3 excluded. From Eq. (6c), the constraint on the

Optics EXPRESS

coefficients to be determined on the reflective surface Γ_3 can be obtained

$$x = Px', \tag{8}$$

where $x' = \begin{bmatrix} x^1_{\Omega_1-\Gamma_3} & x^1_{\Gamma_3} & x^2_{\Omega_2-\Gamma_3} \end{bmatrix}^T$, the transformation matrix $P = \begin{bmatrix} I & 0 & 0 \\ 0 & I & 0 \\ 0 & 0 & I \\ 0 & -Ie^{-i(\phi^1-\phi^2)} & 0 \end{bmatrix}$, I is the identity matrix. By using matrix operations and Eq. (8), Eq. (7) can be rewritten as [8]

$$P^{\dagger}APx' = P^{\dagger}b, \tag{9}$$

where $P^{\dagger}$ is the Hermitian conjugate of P. By solving Eq. (9), the scattered electric field for reflection can be obtained. In the reflection scenario, domain division is a critical step. Each subdomain must contain beams propagating in a single direction. If necessary, a limited number of rays can be traced to facilitate this process. Since RWM utilizes a single type of multi-scale basis function within each subdomain, with the exception of overlapping domains that incorporate two types of basis functions, the total number of DOFs does not significantly increase compared to the refraction case.

2.3. Diffraction

The diffraction scenario is inherently complex. When a single beam traverses a diffractive device, it generates new beams corresponding to different diffraction orders. The propagation phase of these diffraction orders cannot be directly calculated using the FIM. Instead, numerical methods such as RCWA and the grating equation are employed to determine the propagation phase $\phi_0(\boldsymbol{r})$ at the exit surface Γ_3 of the diffractive device. Only after deriving $\phi_0(\boldsymbol{r})$ can FIM be utilized to compute the propagation phase across the entire computational domain. As depicted in Fig. 1(d), constructing multi-scale basis functions in the diffraction scenario involves three steps. First, calculate the propagation phase $\phi_0(\boldsymbol{r})$ at the exit surface Γ_3 using the incident beam, the structure of the diffractive device, and other numerical methods. Second, employ FIM to compute the propagation phase $\phi^2(\boldsymbol{r})$ in the non-diffraction region Ω_2 based on $\phi_0(\boldsymbol{r})$. Since the FIM cannot accurately resolve $\phi^1(\boldsymbol{r})$ within the diffraction region Ω_1, we set $\phi^1(\boldsymbol{r})$ to zero there, which introduces a discontinuity in the propagation phase on Γ_3. Finally, construct multi-scale basis functions $\boldsymbol{M}^1_j(\boldsymbol{r}) = \boldsymbol{N}^1_j(\boldsymbol{r})e^{-i\phi^1(\boldsymbol{r})}$ and $\boldsymbol{M}^2_j(\boldsymbol{r}) = \boldsymbol{N}^2_j(\boldsymbol{r})e^{-i\phi^2(\boldsymbol{r})}$ to discretize the electric field $\boldsymbol{E}^1(\boldsymbol{r}) = \sum_{j=1}^{N_1} e^1_j \boldsymbol{M}^1_j(\boldsymbol{r})$ in Ω_1 and $\boldsymbol{E}^2(\boldsymbol{r}) = \sum_{j=1}^{N_2} e^2_j \boldsymbol{M}^2_j$ in Ω_2.

After constructing the multi-scale basis functions, the implementation of RWM for the diffraction problem is the same as for the refraction problem. As shown in Fig. 1(d), Ω is also the computational domain, and the boundary Γ consists of Γ_1, Γ_2 and Γ_3. The derivation of the assembly matrix also incorporates examples of SBC on Γ_2 and plane wave incident excitations on Γ_1. To address the discontinuity of the propagation phase on Γ_3, we impose the Robin Transmission Boundary Condition (RBC),

$$\boldsymbol{n} \times \boldsymbol{\mu}_r^{-1} \nabla \times \boldsymbol{E}^1(\boldsymbol{r}) - ik_0 \boldsymbol{\epsilon}_r \boldsymbol{n} \times \boldsymbol{E}^1(\boldsymbol{r}) \times \boldsymbol{n} = \boldsymbol{n} \times \boldsymbol{\mu}_r^{-1} \nabla \times \boldsymbol{E}^2(\boldsymbol{r}) - ik_0 \boldsymbol{\epsilon}_r \boldsymbol{n} \times \boldsymbol{E}^2(\boldsymbol{r}) \times \boldsymbol{n}, on \quad \Gamma_3 \tag{10}$$

Equation (10) integrates the continuity conditions of both electric and magnetic fields, embodying a local impedance matching relationship that simulates the propagation of electric fields between two distinct regions.

Optics EXPRESS

By applying the standard finite element procedure, the assembly matrix is derived as

$$\begin{bmatrix} A^1 + K^1 + R^1 & R^2 \\ R^3 & A^2 + K^2 + R^4 \end{bmatrix} \begin{bmatrix} x^1 \\ x^2 \end{bmatrix} = \begin{bmatrix} b^1 \\ 0 \end{bmatrix}, \tag{11}$$

where the meaning of $A^1/A^2/K^1/K^2/b^1/x^1/x^2$ and the form of the matrix elements are the same as in the previous subsection. The elements of coupling matrix terms are

$$\begin{cases} R^1_{ij} = \int_{\Gamma_3} [ik_0\boldsymbol{\epsilon}_r(\boldsymbol{n} \times (\boldsymbol{M}^1_i)^*) \cdot (\boldsymbol{n} \times \boldsymbol{M}^1_j)]dS, \\ R^2_{ij} = \int_{\Gamma_3} [(\boldsymbol{M}^1_i)^* \cdot (\boldsymbol{n} \times \boldsymbol{\mu}_r^{-1}\nabla \times \boldsymbol{M}^2_j) - ik_0\boldsymbol{\epsilon}_r(\boldsymbol{n} \times (\boldsymbol{M}^1_i)^*) \cdot (\boldsymbol{n} \times \boldsymbol{M}^2_j)]dS, \\ R^3_{ij} = \int_{\Gamma_3} [(\boldsymbol{M}^2_i)^* \cdot \boldsymbol{n} \times \boldsymbol{\mu}_r^{-1}\nabla \times \boldsymbol{M}^1_j) - ik_0\boldsymbol{\epsilon}_r(\boldsymbol{n} \times (\boldsymbol{M}^2_i)^*) \cdot (\boldsymbol{n} \times \boldsymbol{M}^1_j)]dS, \\ R^4_{ij} = \int_{\Gamma_3} [ik_0\boldsymbol{\epsilon}_r(\boldsymbol{n} \times (\boldsymbol{M}^2_i)^*) \cdot (\boldsymbol{n} \times \boldsymbol{M}^2_j)]dS. \end{cases}$$

By solving Eq. (9), the scattered electric field for diffraction can be obtained.

3. Numerical examples

In this section, the accuracy and efficacy of RWM are demonstrated through three numerical examples and compared with the standard FEM. The relative error between RWM and the standard FEM results is calculated using the following equation,

$$\text{error} = \sqrt{\frac{\sum_{i=1}^{N} \|E_i - E_{0i}\|^2}{\sum_{i=1}^{N} \|E_{0i}\|^2}}, \tag{12}$$

where E_{0i}/E_i is the electric field obtained from FEM/RWM, the subscript i represents the value at the i-th mesh vertex, N is the total number of vertices. All results are obtained from a local server equipped with a 96-core CPU and 1548 GB of RAM. It should be noted that the results from the standard FEM were obtained using the commercial software COMSOL. In the following examples, the RWM results will be compared with those from COMSOL. In this method, the mesh density ($\sqrt{3}$ times the radius of the circumscribed circle of the mesh) for FIM is set to 10λ, where λ is the wavelength. For FEM, which employs the second-order basis functions, the mesh density is set between λ and $\lambda/2$ to ensure convergence and obtain accurate results. For more details on convergence, please refer to Refs. [9,22].

3.1. Double-slit Interference

First, we use the simple example of double-slit interference to illustrate the effectiveness of RWM with physics-informed multi-scale basis functions. As shown in Fig. 2(a), two Gaussian beams with a wavelength of 1 μm and a beam waist radius of 1 μm are incident from two elongated waveguides into a square region. The incident boundaries are indicated by red lines in the figure, corresponding to the boundary condition associated with Γ_1 and Γ_2 in Section 2.1, respectively. The purple dashed line in the figure denotes the SBC, corresponding to the boundary condition represented by Γ_3 in Section 2.1. The system has overall dimensions of 60 μm by 60 μm, the refractive index of the entire region is 1, and the region boundaries are surrounded by PML.

Figure 2(b) displays the electric field simulation results obtained using RWM and the standard FEM. The standard FEM employs a mesh density of $\lambda/5$, utilizing 232,902 mesh elements. In contrast, RWM uses a mesh density of λ, requiring only 9,744 mesh elements. The

Optics EXPRESS

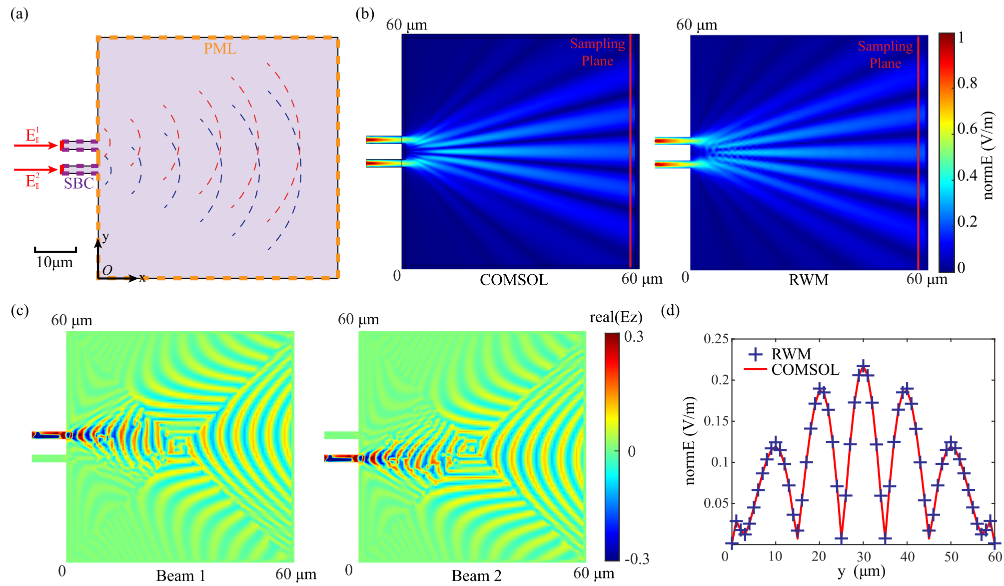

Fig. 2. Computational results of the double-slit interference. (a) Model structure. (b) Electric fields simulation results of FEM and RWM. (c) Electric fields simulation results for the real parts of two beams by RWM. (d) Comparison of electric fields simulated by RWM and FEM at the sampling plane.

comparison between the electric fields indicates that the simulation results from both methods are fundamentally consistent. Furthermore, the relative error between the two electric fields is 0.0826, calculated according to Eq. (12). Figure 2(c) shows the real parts of electric field distributions of Beam 1 and Beam 2, respectively. The electric field distribution on the left (right) agrees well with the distribution when only Gaussian beam 1 (2) is incident. This accurately corresponds to interference physics phenomena, as coherent light waves do not interact but merely superimpose their electric fields. Consequently, the electric field calculation of beam 1 should be identical no matter whether the incident beam 2 is absent or not. Figure 2(d) further compares the electric field intensity of the two methods on the sampling plane, specifically along the red line indicated in Fig. 2(b). The peaks and troughs of the interference fringes obtained from the RWM simulation show remarkable alignment with those from the FEM.

The summary of computational resource usage and relative error for the two methods is presented in Table 1. Although RWM requires the use of two types of multi-scale basis functions to discretize the dual beams, its DOFs are only one-twelfth of those of the standard FEM. Moreover, it achieves a computational speed that is 20 times faster, thereby fully demonstrating the high efficiency of this method.

Table 1. Numerical comparison of RWM and FEM for the double-slit interference

Methods	Degree of Freedom	Computational Time	Memory Consumption	Relative Error
FEM	467,185	28.1s	4.25GB	-
RWM	39,530	1.3s	1.97GB	0.0826

Optics EXPRESS

3.2. Freeform-surface off-axis reflective optical system

Freeform off-axis reflective optical systems significantly enhance imaging quality and energy efficiency by eliminating the central obstruction problem inherent in traditional coaxial reflective systems. By using the precise and asymmetric wavefront phase control offered by freeform surfaces [31], these systems provide advantages such as a wide field of view and high resolution. They are extensively used in advanced optical engineering fields, including space astronomy observation [32], high-resolution Earth remote sensing [33], and virtual and augmented reality [34–36]. We use an off-axis three-mirror optical system composed of freeform mirrors to further illustrate the benefits of RWM in multi-scale optical systems. This example is based on the structure from a paper [37] and is scaled down to fit within the simulation range of RWM, as shown in Fig. 3(a). A Gaussian beam with a wavelength of 1500 nm and a waist radius of 80μm is incident horizontally and is sequentially reflected by three freeform mirrors, ultimately focusing on the focal plane. The freeform mirrors are described using a polynomial form,

$$x = \frac{cy^2}{1 + \sqrt{1 - (1+k)c^2y^2}} + \sum_{i=1}^{N} A_i E_i(y). \tag{13}$$

The first term describes the conic surface, where c represents the curvature at the vertex, with $c = 1/R$, R is the radius of curvature, and k denotes the conic constant. The latter term describes the polynomial surface, where A_i is the coefficient of the ith polynomial term, and $E_i(y)$ can represent various polynomials such as Zernike polynomials or power series. In this example, power series terms from the 1st to the 3rd order are selected. The parameters for the three freeform reflective mirrors are shown in Table 2, with negative values of the radius of curvature indicating that the radial direction is opposite to the direction of the incident beam. Assuming the mirrors can fully reflect the incident light and the PEC boundary condition is applied in RWM modeling.

Table 2. System parameters of the reflective optical system

Surface	Curvature Radius/mm	Conic Constant	y-term Coefficient	y^2-term Coefficient	y^3-term Coefficient
Mirror 1	-4.22	-1.21	-5.2×10^{-5}	8.6×10^{-7}	-5.5×10^{-10}
Mirror 2	-0.5	0	-1.3×10^{-4}	3.8×10^{-6}	-5.7×10^{-9}
Mirror 3	-1.04	-3.08	1.0×10^{-4}	2.9×10^{-7}	2.5×10^{-10}

The entire simulation domain, measuring about 1100 μm by 900 μm, is divided into four subdomains. Figure 3(b) displays the electric field intensity distributions obtained from RWM and standard FEM. Figure 3(c) shows the electric field results in the four subdomains, demonstrating that the electric field in each subdomain can be accurately simulated. Figure 3(d) shows the comparison of electric fields simulated by RWM and standard FEM at the focal plane, which is indicated by the red solid line in the lower left corner of Fig. 3(a). The results demonstrate that the electric field obtained via RWM closely matches that of FEM in both the primary peak and the secondary peak.

Table 3 provides the computational resource usage and relative errors of the two methods. RWM uses a mesh with a density of $\lambda/1.2$ and requires 3,520,060 DOFs, while FEM uses a finer mesh density of $\lambda/5$, resulting in 47,375,142 DOFs. Compared to standard FEM, RWM reduces memory usage to one-eighth and increases computational speed by 21 times, with a relative error of only 0.13. All calculations were performed on a local server equipped with 1548 GB of memory, ensuring that the memory usage of standard FEM did not reach the memory wall. As the size of the optical system increases and approaches the memory wall limit, the computational advantage of RWM will become even more significant.

Optics EXPRESS

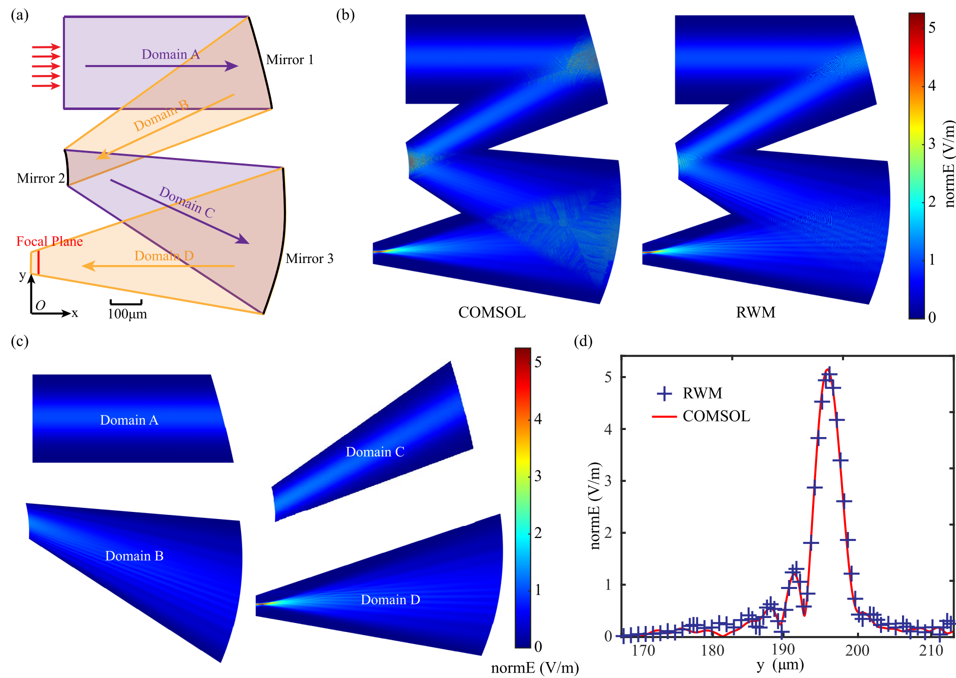

Fig. 3. Computational results of the off-axis reflective system. (a) Model structure. (b) Electric fields simulation results of FEM and RWM. (c) Electric fields simulation results for four subdomains by RWM. (d) Comparison of electric fields simulated by RWM and FEM at the focal plane.

Table 3. Numerical comparison of RWM and FEM for the reflective optical system

Methods	Degree of Freedom	Computational Time	Memory Consumption	Relative Error
FEM	47,375,142	1389s	135.83GB	-
RWM	3,520,060	65s	17.6GB	0.1376

3.3. Refractive-diffractive hybrid optical system

Finally, we illustrate the potential of RWM in complex multi-scale optical systems through an example featuring a refractive-diffractive hybrid optical system [38–41], which consists of a diffraction grating and lenses.The optical system illustrated in Fig. 4(a) comprises a 50-element grating and a cemented doublet lens. A Gaussian beam is incident horizontally from the left side of the system, with a wavelength of 500 nm and a waist radius of 40 μm. The refractive index of the coating on the grating is 2.0, while the refractive indices of Lens 1 and Lens 2 are 1.68 and 1.65, respectively. The overall size of the system is 100 μm $\times$ 230 μm. To reduce stray light from Fresnel reflections, anti-reflective coatings are applied to the lens surfaces, as indicated by Film 1 and Film 2 in Fig. 4(a).

Figure 4(b) displays the electric field intensity distributions obtained from RWM and the standard FEM. The upper part of the figure presents the simulation results from RWM, wherein the grating region utilizes a mesh density of $\lambda/6$ while the lens region employs a mesh density of $\lambda/1.5$, with a graded transition mesh interfacing the two regions. The two regions are coupled via RBC, as indicated by the blue line in Fig. 4(a). In contrast, the bottom translucent half displays

Optics EXPRESS

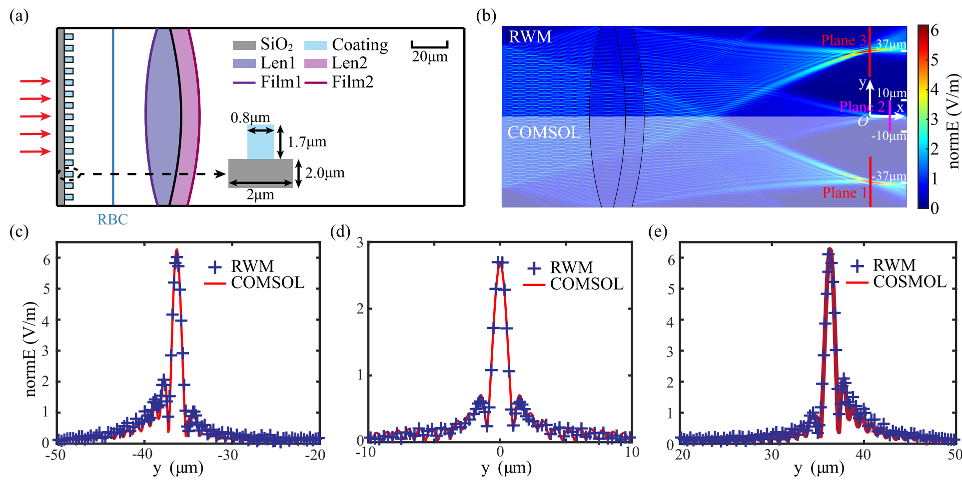

Fig. 4. Computational results of refractive-diffractive hybrid optical system. (a) Model structure. (b) Electric fields simulation results of FEM and RWM. (c)–(e) Comparison of electric fields simulated by RWM and FEM at the focal plane of the three orders.

the simulation results of standard FEM, which uses a mesh density of $\lambda/6$. Figure 4(c) presents the comparison curves of the electric field results for three diffraction orders simulated by RWM and FEM. From left to right, these correspond to the -1st order, 0th order, and +1st order electric fields, respectively. It is evident that the simulation results from both methods exhibit an excellent match for the primary and secondary peaks of the electric field distribution for the three orders.

Table 4 also presents the computational resource usage and relative errors of the two methods. The DOFs for RWM are 3,050,766, with the grating region requiring 1,464,749 DOFs to ensure simulation accuracy due to its zero-phase distribution, while the lens region employs 1,585,997 DOFs. In contrast, FEM uses 18,238,285 DOFs, which is six times that of RWM. Compared to the standard FEM, RWM improves computational time by a factor of 9 and reduces memory usage to one-fifth, with an error of only 0.1546. This confirms the effectiveness and efficiency of RWM in complex optical systems.

Table 4. Calculation information of RWM and FEM for refractive-diffractive hybrid optical system

Methods	Degree of Freedom	Computational Time	Memory Consumption	Relative Error
FEM	18,238,285	581s	58.98GB	-
RWM	3,050,766	60.3s	11.9GB	0.1546

4. Conclusion

In conclusion, this work extends RWM combined physics-informed information to accurately simulate strong wave phenomena, such as reflection and diffraction, in complex multi-scale optical systems. In these systems, where multiple beams overlap and evolve, the phase distribution cannot be directly obtained using the geometrical optics method, and the electric field cannot be discretized accurately with a single type of multi-scale basis function. Consequently, we developed various processing approaches tailored to the physical characteristics of different strong wave effects. These approaches enable the construction of suitable multi-scale basis functions and the precise discretization of the electric field distribution. Numerical simulations of double-slit

Optics EXPRESS

interference, off-axis three-mirror systems, and refractive-diffractive hybrid systems validate the accuracy and efficiency of the improved method. This method is applicable to various scenarios, including refraction, self-focusing, interference, reflection, and diffraction, and the treatment of these phenomena is mutually compatible within the same framework. We believe that this improved method represents significant progress in the simulation and modeling of multi-scale optical systems and has the potential to facilitate integrated, precise, and efficient simulations of real-world multi-scale optical systems, thereby aiding researchers in their analysis and design.

Funding. National Natural Science Foundation of China (62535007); Natural Science Foundation of Hubei Province (2024AFA016); Innovation Project of Optics Valley Laboratory.

Disclosures. The authors declare that there is a potential conflict of interest regarding the work described in this paper. Yuntian Chen, Jingwei Wang and Fan Xiao have filed two patents related to the method discussed in this paper. The patents are currently under review. The details of the patent application are as follows: CN202410681037.9 and CN202410681079.2. These patents have not influenced the representation or interpretation of the reported research results.

Data availability. Data underlying the results presented in this paper are not publicly available at this time but may be obtained from the authors upon reasonable request.

References

1. Y. Ding, Q. Yang, Y. Li, *et al.*, "Waveguide-based augmented reality displays: perspectives and challenges," eLight **3**(1), 24 (2023).
2. J. Xiong, E.-L. Hsiang, Z. He, *et al.*, "Augmented reality and virtual reality displays: emerging technologies and future perspectives," Light:Sci. Appl. **10**(1), 216 (2021).
3. J. Zou, T. Zhan, E.-L. Hsiang, *et al.*, "Doubling the optical efficiency of vr systems with a directional backlight and a diffractive deflection film," Opt. Express **29**(13), 20673–20686 (2021).
4. J. P. Rolland and J. Goodsell, "Waveguide-based augmented reality displays: a highlight," Light:Sci. Appl. **13**(1), 22 (2024).
5. N. Li, C. P. Ho, J. Xue, *et al.*, "A progress review on solid-state lidar and nanophotonics-based lidar sensors," Laser & Photonics Reviews **16**(11), 2100511 (2022).
6. I. Kim, R. J. Martins, J. Jang, *et al.*, "Nanophotonics for light detection and ranging technology," Nat. Nanotechnol. **16**(5), 508–524 (2021).
7. A. Taflove, S. C. Hagness, and M. Piket-May, "Computational electromagnetics: the finite-difference time-domain method," *The Electrical Engineering Handbook* Vol. 3 (2005), p. 15.
8. J. M. Jin, *The Finite Element Method in Electromagnetics* (John Wiley & Sons, 2015).
9. J. Wang, Z. Wang, L. Liu, *et al.*, "Multi-scale multi-domain hybrid finite element modeling of light propagation," Electromag. Sci. **2**(4), 1–10 (2024).
10. J. Qin, Q. Song, X. Liu, *et al.*, "Domestic 3d visualization diffractive waveguide simulation module based on ray-field tracing," Chinese Optics **18**, 1–12 (2026).
11. C. Leiner, W. Nemitz, S. Schweitzer, *et al.*, "Multiple interfacing between classical ray-tracing and wave-optical simulation approaches: a study on applicability and accuracy," Opt. Express **22**(13), 16048–16060 (2014).
12. Z. Lokar, B. Lipovsek, A. Razzaq, *et al.*, "Coupled modelling approach for optimization of bifacial silicon heterojunction solar cells with multi-scale interface textures," Opt. Express **27**(20), A1554–A1568 (2019).
13. R. Shi, C. Hellmann, and F. Wyrowski, "Physical-optics propagation through curved surfaces," J. Opt. Soc. Am. A **36**(7), 1252–1260 (2019).
14. R. Shi, N. Janunts, C. Hellmann, *et al.*, "Vectorial physical-optics modeling of fourier microscopy systems in nanooptics," J. Opt. Soc. Am. A **37**(7), 1193–1205 (2020).
15. R. Shi, Z. Wang, S.-T. Hung, *et al.*, "Numerical analysis of tiny-focal-spot generation by focusing linearly, circularly, and radially polarized beams through a micro/nanoparticle," Opt. Express **29**(2), 2332–2347 (2021).
16. C. Leiner, S. Schweitzer, V. Schmidt, *et al.*, "Multi-scale simulation of an optical device using a novel approach for combining ray-tracing and FDTD," Proc. SPIE **8781**, 87810Z (2013).
17. C. Leiner, W. Nemitz, F. P. Wenzl, *et al.*, "A simulation procedure for light-matter interaction at different length scales," Proc. SPIE **8429**, 84290L (2012).
18. C. Leiner, S. Schweitzer, F.-P. Wenzl, *et al.*, "A simulation procedure interfacing ray-tracing and finite-difference time-domain methods for a combined simulation of diffractive and refractive optical elements," J. Lightwave Technol. **32**(6), 1054–1062 (2014).
19. Z. Lokar, B. Lipovsek, J. Krc, *et al.*, "Performance analysis of rigorous coupled-wave analysis and its integration in a coupled modeling approach for optical simulation of complete heterojunction silicon solar cells," Beilstein J. Nanotechnol. **9**, 2315–2329 (2018).
20. F. Wyrowski and M. Kuhn, "Introduction to field tracing," J. Mod. Opt. **58**(5-6), 449–466 (2011).
21. M. Kuhn, F. Wyrowski, and C. Hellmann, "Non-sequential optical field tracing," in *Advanced Finite Element Methods and Applications* (Springer, 2013), pp. 257–273.

22. F. Xiao, J. Wang, Z. Xiong, *et al.*, "Numerical approximation of slowly varying envelope in finite element electromagnetism: a ray-wave method of modeling multi-scale devices," Opt. Express **33**(6), 12603–12614 (2025).
23. M. Raissi, P. Perdikaris, and G. Karniadakis, "Physics-informed neural networks: A deep learning framework for solving forward and inverse problems involving nonlinear partial differential equations," J. Comput. Phys. **378**, 686–707 (2019).
24. J. Lim and D. Psaltis, "MaxwellNet: Physics-driven deep neural network training based on Maxwell's equations," APL Photonics **7**(1), 011301 (2022).
25. M. Chen, R. Lupoiu, C. Mao, *et al.*, "High Speed Simulation and Freeform Optimization of Nanophotonic Devices with Physics-Augmented Deep Learning," ACS Photonics **9**(9), 3110–3123 (2022).
26. G. Wen, Z. Li, K. Azizzadenesheli, *et al.*, "U-fno—an enhanced fourier neural operator-based deep-learning model for multiphase flow," Adv. Water Resour. **163**, 104180 (2022).
27. Q. Tao, Y. Su, C. Tao, *et al.*, "Efficient method for modeling large-scale arrays of optical nanoresonators based on the coupling theory of quasinormal mode," Opt. Express **32**(5), 7171–7184 (2024).
28. W.-K. Jeong and R. T. Whitaker, "A fast iterative method for eikonal equations," SIAM J. Sci. Comput. **30**(5), 2512–2534 (2008).
29. Z. Fu, W.-K. Jeong, Y. Pan, *et al.*, "A fast iterative method for solving the eikonal equation on triangulated surfaces," SIAM J. Sci. Comput. **33**(5), 2468–2488 (2011).
30. Z. Fu, R. M. Kirby, and R. T. Whitaker, "A fast iterative method for solving the eikonal equation on tetrahedral domains," SIAM J. Sci. Comput. **35**(5), C473–C494 (2013).
31. J. P. Rolland, M. A. Davies, T. J. Suleski, *et al.*, "Freeform optics for imaging," Optica **8**(2), 161–176 (2021).
32. Z. Challita, T. Agócs, E. Hugot, *et al.*, "Design and development of a freeform active mirror for an astronomy application," Opt. Eng. **53**(3), 031311 (2014).
33. Y. Liu, A. Bauer, T. Viard, *et al.*, "Freeform hyperspectral imager design in a cubesat format," Opt. Express **29**(22), 35915–35928 (2021).
34. T. Yang, J. Zhu, W. Hou, *et al.*, "Design method of freeform off-axis reflective imaging systems with a direct construction process," Opt. Express **22**(8), 9193–9205 (2014).
35. J. Ye, L. Chen, X. Li, *et al.*, "Review of optical freeform surface representation technique and its application," Opt. Eng. **56**(11), 1–110901 (2017).
36. S. Wei, Z. Fan, Z. Zhu, *et al.*, "Design of a head-up display based on freeform reflective systems for automotive applications," Appl. Opt. **58**(7), 1675–1681 (2019).
37. Z. Qian, H. Ji, R. Fan, *et al.*, "Aberration compensation design method of freeform reflection systems based on generalized aberration theory with series expansion," Opt. Express **33**(10), 20664–20681 (2025).
38. Y. Fu and N. K. A. Bryan, "Design of hybrid micro-diffractive-refractive optical element with wide field of view for free space optical interconnections," Opt. Express **10**(13), 540–549 (2002).
39. S. Mao and J. Zhao, "Design and analysis of a hybrid optical system containing a multilayer diffractive optical element with improved diffraction efficiency," Appl. Opt. **59**(20), 5888–5895 (2020).
40. J. Amako and H. Nakano, "Achromatic optical system with diffractive-refractive hybrid lenses for multifocusing of ultrashort pulse beams," Opt. Express **29**(3), 4488–4503 (2021).
41. Y. Wang, J. Li, X. Hou, *et al.*, "Hybrid diffractive-refractive lens for chromatic confocal measurement system," Opt. Express **32**(11), 20128–20135 (2024).